Applied
Ceramic
TECHNOLOGY

Niobium oxide-activated yttrium barium titanate nanorod structured ceramics for energy storage applications

Ravanamma Rallapalli[1] | **Muralidhara Reddy Kalimi**[2] | **Ravi Nirlakalla**[2] |
Padma Suvarna Reniguntla[1]

[1]Department of Physics, Jawaharlal Nehru Technological University Anantapur, Anantapuramu, India

[2]Department of Physics, Rajeev Gandhi Memorial College of Engineering and Technology, Nandyal, India

Correspondence
Ravi Nirlakalla, Department of Physics, Rajeev Gandhi Memorial College of Engineering and Technology, Nandyal 518501, India.
Email: ravi2728@gmail.com

Abstract

Structure, morphology, and electrical properties of 10 mol% of Nb_2O_5-activated yttrium barium titanate (BT) $Ba_{(60-z)}Ti_{(40-x)}Nb_zY_xO_3$ ($BTY_{10}Nb_{10}$), barium titanate (BT), and 10 mol% of Y_2O_3-activated BT were explored with calcination and sintering temperatures of 1000°C at 8 h and 1200°C at 6 h, respectively. The thermogravimetric and differential scanning calorimetry (TG–DSC) analysis reported that the total weight loss and residual mass of BT at 1300°C were 16.8 and 83.2%, respectively. The X-ray diffraction (XRD) pattern confirmed that $BTY_{10}Nb_{10}$ ceramics containing the $BaNbO_3$ phase were developed. A Raman band of BT at 307 cm^{-1} unveiled a blue shift slightly for BTY_{10} to 298 cm^{-1} and for $BTY_{10}Nb_{10}$ to 306 cm^{-1}. Average pore area of the ferroelectric $BTY_{10}Nb_{10}$ was found to be 6.96 nm for the total scanning electron microscopy (SEM) image area of 20.31 nm. Formation of BT nanorods analyzed from transmission electron microscopy (TEM) has been reported in three samples that regulate surface roughness. Moreover, Nyquist diagram of $BTY_{10}Nb_{10}$ shows two overlapping semicircles as a function of frequency. Nanorod structures led to change the morphology and surface roughness. Recoverable energy storage density and energy storage efficiency were estimated as 2.63 $\mu J/cm^3$ and 57%, and $BTY_{10}Nb_{10}$ ferroelectric showed potential for energy storage applications due to changes in surface morphology and porosity.

KEYWORDS
barium titanate, dielectric properties and energy storage, niobium oxide, structure, yttrium oxide

1 | INTRODUCTION

The most promising dielectric properties are high dielectric constant, tangential low dielectric loss, dielectric reliability, high electromechanical coupling coefficient, and excellent resistance to thermal shock usually exhibit by barium titanate—$BaTiO_3$ (BT). Electrical energy storage (EES) is necessary for the power supply of portable electronics and additional renewable energy technolo-gies. Modern commercial EES devices take into account batteries, dielectric capacitors, and supercapacitors. In particular, solid-state dielectric capacitors have a high power density, a very high operating voltage, and a long life cycle.[1,2] This has led researchers to focus on dielectric capacitors with high energy density and very high charge/discharge rates in recent years. However, the energy storage capacity of dielectric capacitors is usually low. In the future, the high energy storage density

and efficiency of dielectric capacitors will meet the requirements of advanced electrical and electronic systems for reduction. In general, there are three categories of ceramic materials that are practical in the field of dielectric capacitors: linear dielectrics, antiferroelectric, and ferroelectric.[3]

The recoverable energy storage density (W_{rec}) of a dielectric material is generally evaluated by incorporating the effective cross-sectional area between the polarization axis and the discharge curve of the polarization–electric field (P–E) hysteresis loops. This W_{rec} of dielectric capacitors can be calculated using Equation (1)[4–6]:

$$W_{rec} = \int_{P_r}^{P_{max}} E \, dP \tag{1}$$

where P, P_{max}, and P_r are the polarization value at an electric field (E), the saturated polarization, and the remanent polarization, respectively. Therefore, large P_{max} and huge dielectric breakdown strength (BDS) along with small P_r are significant to evaluate prominent energy storage performance. Moreover, the energy storage efficiency (η) is assessed using Equation (2)[7]:

$$\eta = \frac{W_{rec}}{W_{rec} + W_{loss}} \times 100\% \tag{2}$$

where W_{loss} is the hysteresis loss.

In general, due to bipolar polarization, ferroelectric materials have a high dielectric constant. In the future, these materials are widely studied for electrostatic capacitors. Applying the principle of high electric field to enhance the dielectric response increases the hysteresis. This phenomenon works in parallel with the reduction of energy storage density that can be achieved with ferroelectric materials. Therefore, high energy density ferroelectric capacitors are usually achieved by reducing the dielectric hardness of the material or by reducing the dielectric hysteresis loss.[8] BT-based ferroelectric ceramics as the typical ferroelectric material of perovskite structures have always been a fascinating curiosity in progressive energy storage applications.

The substitution of yttrium oxide (Y_2O_3) at the Ba^{2+} sites has been extensively used to tailor the positive temperature coefficient effect in semiconducting BT, which establishes the occupancy of Y^{3+} at the Ba^{2+} sites of BT. Conductivity measurements and microstructure examinations confirmed that the Y^{3+} ion position of BT depends on the Ba/Ti ratio, but not on the partial pressure of oxygen.[9] However, BT is essentially an insulator and can be converted into a semiconductor by adding a donor dopant. As these dopants cause charge imbalances, they create vacancies to maintain charge neutrality. Donor doping Nb^{5+} for Ti site is advantageous to fill up the oxygen vacancies and suppress

oxide ion conduction. Nb^{5+} is a donor impurity in the BT network that causes sample charge imbalances and produces n-type semiconductors. Therefore, charge compensation requires formation of vacancies at A site in the lattice, that is, barium and titanium vacancies to increase the contribution of the domain wall to permeability as a result of the large number of domain walls.[10] The addition of Nb to BT generates electrons, holes, and/or vacancies. However, the solubility of Nb in BT depends on the particle size of the powder and the Nb content improves the activation energy.

In this paper, Nb_2O_5-doped $YBaTiO_3$, Y_2O_3-doped $BaTiO_3$, and bare $BaTiO_3$ ferroelectric ceramics were prepared by conventional solid-state reaction process. Y^{3+} and Nb^{5+} ions in BT are explored for energy storage applications with thermal analysis (thermogravimetric and differential scanning calorimetry [TG–DSC], structure (X-ray diffraction [XRD], fourier transform infrared spectroscopy [FTIR], and Raman spectroscopy), morphology (scanning electron microscopy [SEM] and transmission electron microscopy [TEM]), frequency-dependent dielectric properties, and electric hysteresis.

2 | MATERIALS AND METHODS

2.1 | Experimental procedure

Solid raw materials were utilized to synthesize $BaTiO_3$ (BT), Y_2O_3-doped $BaTiO_3$ (BTY), and Nb_2O_5-doped yttrium-based $BaTiO_3$ (BTYNb) by conventional solid-state reaction route under air atmosphere from 99% barium carbonate ($BaCO_3$), 99% titanium dioxide (TiO_2), 99% yttrium oxide (Y_2O_3), and 99% niobium pentoxide (Nb_2O_5) procured from Sigma Aldrich. A batch of 10 g of powder mixture of BT, BTY, and BTYNb was prepared in the exact stoichiometric ratio.

1. $60BaO + 40TiO_2 = BaTiO_3$ (BT);
2. $60BaO + (40 - x)TiO_2 + xY_2O_3 = BaTi_{(40-x)}O_3Y_x$ (BTY), where x = 2, 4, 6, 8, 10, and 15;
3. $(60 - z)BaO + (40 - x)TiO_2 + xY_2O_3 + zNb_2O_5 = Ba_{(60-z)}Ti_{(40-x)}O_3Nb_zY_x$ (BTY$_{10}$Nb$_{10}$), where x = 10 and z = 10.

Powder mixtures weighed at various concentrations of Y_2O_3 were heated at 400°C for 1 h to evaporate the carbon dioxide (CO_2) and other hydroxyl groups. Using an agate mortar and a pestle in ethanol medium, each composition was ground for 12 h to give a homogeneous fine powder. In addition, these compositions were calcined using an electric oven heated to 1000°C for 8 h. Then cooled to room temperature at a rate of 4°C/min. To these calcined

powders, .5% by weight of paraffin was added as a binder at room temperature, and when hydraulic pressure of 10 MPa was applied, several thin cylindrical discs were prepared in a steel mold. In addition, these pellets were annealed at 500°C for 1 h to remove the binder from the sample. The discs were sintered at a constant temperature of 1200°C for 6 h at a heating and cooling rate of 4°C/min. Finally, the samples were subjected to the polishing process to obtain a flat surface and a conductive silver paste was used to achieve reliable metal contact. In addition, the discs were heated to 400°C to provide a good interface between the materials. Samples were sent in powder and tablet form for further characterizations.

2.2 | Characterization techniques

TG and DSC were analyzed by NETZSCH STA 449 F3 Jupiter in the temperature range 25°C–1400°C. A RIGAKU X-ray diffractometer (Miniflex-600) with $CuK_{\alpha 1}$ radiation source with a wavelength of 1.5405 Å (power: $35\,V \times 15\,mA$) was used to record diffraction pattern of the powder sample. Using JASCO FT/IR-4100 type A spectrometer, FTIR spectra from 500 to 3000 cm^{-1} were recorded. Horiba Jobin Yvon, model number: LabRAM HR Evolution in the range of 50–4000 cm^{-1} was used to obtain micro-Raman with 532 nm laser excitation. SEM images were recorded using the JEOL JSM-IT500 series at 3.0 nm (30 kV) and 15.0 nm (1.0 kV) high vacuum mode resolutions. The particle size and morphology of BT, BTY_{10}, and $BTNb_{10}$ were evaluated with a TEM using a Philips CM 200 with an operating voltage of 20–200 kV and a resolution of 2.4 Å. Dielectric properties of the $BTY_{10}Nb_{10}$ sample were measured using broadband dielectric spectrometer by Novocontrol Technologies, model: Concept 80 Germany, with low/high temperature range –150°C to 900°C having a frequency range of 3 μHz–20 MHz.

3 | RESULTS AND DISCUSSIONS

3.1 | TG–DSC analysis

TG and DSC are performed for uncalcined BT powder in the range 50°C–1300°C to understand the thermal behavior of the material such as weight loss (in%), transition temperature, crystalline temperature including endothermic and exothermic nature. The TG analysis shows the inflection point where the weight of the material begins to decrease rapidly at 911°C in the range of 589°C–964°C as displayed in Figure 1A. This speedy loss of about 15% of mass continued at 934°C and then slowly decreased as the temperature rose to 1300°C. However, total weight loss of

the BT at 1300°C is reported to be 16.8% and the residual mass of BT is 83.2% at the same temperature. Derivative TG, which is a change of mass of BT with time against the temperature, is presented in Figure 1B.

The DSC curve in Figure 1A unveiled two endothermic peaks in which a soft peak was obtained at 374°C and a sharp peak was obtained at 964°C. Evaporation of H_2O molecules, decomposition of thermally unstable organic compounds such as CO_2 and C=O molecules, etc., and evaporation by interacted atmospheric impurities may be caused during a soft first endothermic peak around 374°C.[11–13] During this weight loss, the $BaCO_3$ was decomposed into BaO. Second sharp endothermic peak was identified at 964°C and the weight loss near this temperature was owing to the formation of $BaTiO_3$. Crystalline phase of BT is observed in the temperature range from 814°C to 934°C. Apart from the exothermic crystalline temperature (T_c) peak of 934°C, BT no longer reported significant weight loss due to elevated temperature of up to 1300°C.

3.2 | FTIR spectra

The FTIR spectra of the BT, BTY_{10}, and $BTY_{10}Nb_{10}$ ferroelectric ceramics were recorded in the transmittance mode in the range of 550–3000 cm^{-1} at room temperature as shown in Figure 1C. Vibrational modes of BT were resolved in the infrared spectrum at 545, 655, 749, 862, 1276, 1420, 1753, and 2362 cm^{-1}. On the other hand, samples BTY_2 and BTY_{10} reported bands close to the band of sample BT. However, in general, the vibration modes in the 400–600 cm^{-1} range correspond to the infrared absorption region. There are two strong absorption bands that fall in this region at 545 and 655 cm^{-1} due to vibrations caused by bending and stretching of Ti–O–Ti bond in $[TiO_6]^{2-}$.[14] The 655 cm^{-1} band has shifted to the high frequencies in BTY_2 (688 cm^{-1}), BTY_{10} (661 cm^{-1}), and $BTY_{10}Nb_{10}$ (671 cm^{-1}). Structural deviation in the BT is responsible for this shift. The band at 854 cm^{-1} is attributed to Y–O characteristic band of BTY_2, BTY_{10}, and $BTY_{10}Nb_{10}$, whereas Ti–O band at 862 cm^{-1} is of BT.[15] A stretching vibrational band was perceived at 1276 cm^{-1} corresponding to the symmetric vibrations of [ν_s (COO–)].[16] This is because of the small amount of $BaCO_3$ present in the samples, which is in agreement with the XRD patterns. Moreover, the addition of Y^{3+} ions and Nb^{5+} ions resulted in the shifting of this band to lower frequencies. A small vibrational band perceived at 1420 cm^{-1} for BT is ascribed to asymmetric vibrations of [ν_{as} (COO–)]. In addition, the band observed around 2362 cm^{-1} is owing to the asymmetric vibrations of O=C=O bond of BT, whereas the same band became doublet for BTY_2 and BTY_{10} and shifted to lower frequency
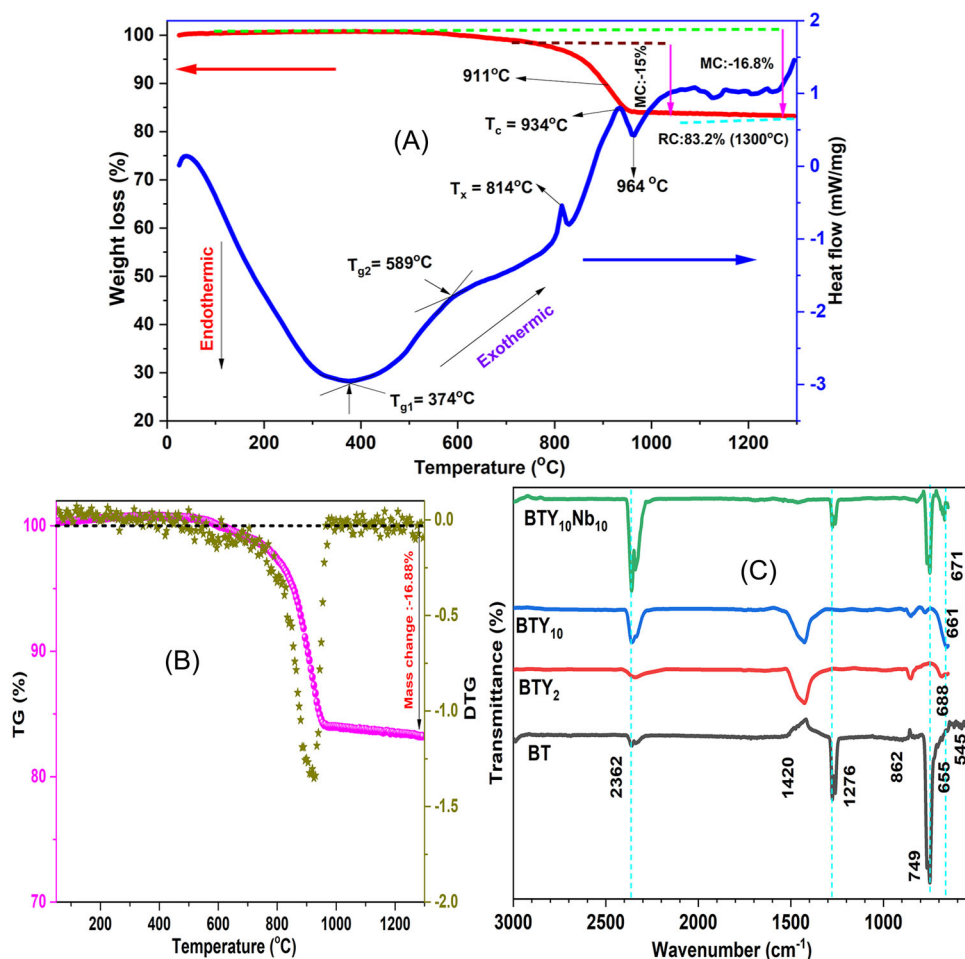
FIGURE 1 Thermogravimetric and differential scanning calorimetry (TG–DSC) curve of BaTiO$_3$: (A) heat flow/weight loss, (B) TG/derivative TG (DTG), and (C) Fourier transform infrared spectroscopy (FTIR) spectra of barium titanate (BT), 2 mol% of Y$_2$O$_3$ doped BT (BTY$_2$), 10 mol% of Y$_2$O$_3$ doped BT (BTY$_{10}$), and 10 mol% of Nb$_2$O$_5$ doped BTY$_{10}$ (BTY$_{10}$Nb$_{10}$).

region. This is due to existence of additional energy levels of dopants. On the other hand, ethanol as a grinding medium also supports to reveal carbon groups in the spectra. Two intense absorption bands were noticed at 749 and 2360 cm^{-1} for 10 mol% of Nb$_2$O$_5$-doped BTY$_{10}$Nb$_{10}$ compared to BT, BTY$_2$, and BTY$_{10}$. Furthermore, the band splitting into doublet at 2360 cm^{-1} is clearly visible in the Nb^{5+}-based BTY$_{10}$Nb$_{10}$ sample.

3.3 | XRD profile

XRD profile of various concentrations of Y$_2$O$_3$-doped BTY and BT is displayed in Figure 2A. A sharp peak of BT is observed at 24.30° with a full width at half maximum (FWHM) of .52 which is ascribed to the composition of BaCO$_3$. In this sample, the highest broad peak with FWHM of about .92 is observed at 34.61°. BTY$_2$ displayed a high intense doublet peak at 30.74° and the corresponding FWHM 1.91. The peak at (110) indices (Ba$_3$Y$_4$O$_9$)

was changed into a singlet when Y$_2$O$_3$ concentration is increased from 2 to 15 mol%. It is interesting to note that as the Y$_2$O$_3$ concentration increases, the peak position shifts to lower angle side. This shift indicates that the increase in inter-planer spacing, resulting in the decrease of lattice strain and elongation of unit cells slightly, leads to the expansion of the crystal structure. A small peak (identified at red arrow in the range 28°–33°) merged with this doublet was located on the left shoulder of the peak, increased the intensity with increasing Y$_2$O$_3$ concentration with expense of the peak on the right shoulder revealed in inset of Figure 2. This is may be due to the more occupation of Y^{3+} ions into the lattice sites of Ba^{2+} and Ti^{4+} ions. An unrevealed doublet was appeared at 42.28° for BTY$_{15}$ because of the higher concentration of Y^{3+} ions as illustrated in the inset of Figure 2A.

The phases of the BTY$_{10}$Nb$_{10}$ composite are TiO$_2$ (01-086-1157), BaTiO$_3$ (01-074-1960), Y$_2$O$_3$ (00-001-0831), BaNbO$_3$ (01-082-1891), Ba$_{12}$Y$_4$Ti$_8$O$_{35}$ (00-043-0417), Ba$_3$Y$_4$O$_9$ (00-027-1037), Y$_{16}$Ti$_{16}$O$_{33}$ (96-200-2732), and
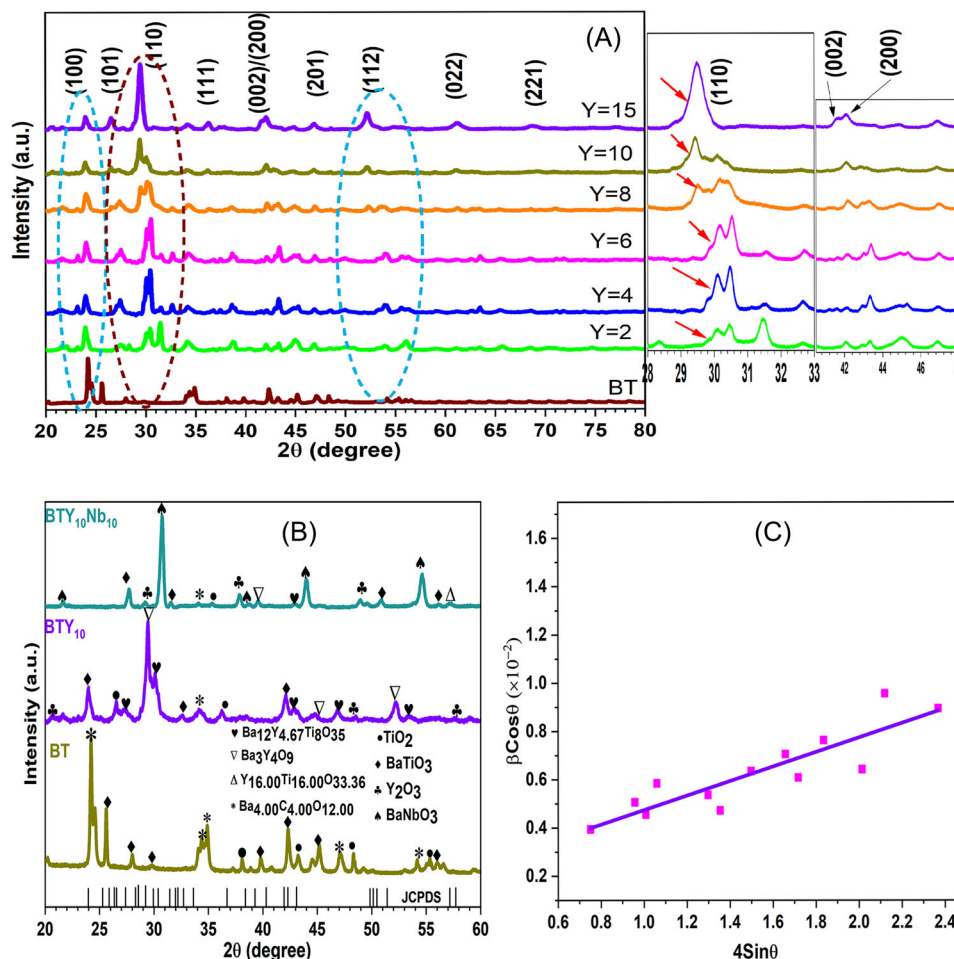
FIGURE 2 X-ray diffraction (XRD) pattern of BT, BTY_{10}, and $BTY_{10}Nb_{10}$ samples. (A) Various concentration of Y_2O_3-doped BT, (B) compound phase identification using JCPDS cards, and (C) Williamson–Hall plot for $BTY_{10}Nb_{10}$ ceramics

$Ba_4C_4O_{12}$ (96-900-6839) (shown in Figure 2B) and are confirmed by using JCPDS files. However, most of the phases related to BT and BTY_{10} phases identified by the JCPDS files are unveiled in Figure 2B. The results from the JCPDS data demonstrate that the BT sample revealed in the $BaTiO_3$ phase, the $Ba_{12}Y_4Ti_8O_{36}$ phase was detected in BTY_{10} sample and $BaNbO_3$ phase was detected in the $BTY_{10}Nb_{10}$ sample.

3.3.1 | Size–strain analysis

The average crystalline size of BT, BTY_{10}, and $BTY_{10}Nb_{10}$ are found to be 26.05, 13.43, and 22.67 nm as evaluated using Sherrer's equation.[17,18] Williamson–Hall (W–H) method is usually assumed to study the influence of strain when evaluating the size of crystals in a sample. The lattice strain in $BTY_{10}Nb_{10}$ leads to the broadening of XRD peaks. The resulting W-H plot disclosed in Figure 2C shows that the line dispersions are predominantly isotropic. This specifies that the diffraction domain is isotropic and micros-

train involvement also exists, which is due to dopant impurities.[19] Slope of the strain $(\varepsilon) = .003 \times 10^{-4}$ value also indicates that the $BTY_{10}Nb_{10}$ was more isotropic and was attributed to small crystallite size.

3.4 | Raman spectral analysis

Raman analysis of BT, BTY_{10}, $BTY_{10}Nb_{10}$ ceramics was performed in the range of 100–1000 cm^{-1} by 532 nm laser excitation. Raman modes split into transverse (TO) and longitudinal (LO) photons due to electrostatic forces in BT associated with lattice ionicity owing to Ba^{2+}. According to crystallography for tetragonal BT crystals the modes are $4E(TO + LO) + 3A_1(TO + LO) + B_1(TO + LO)$. However, $C_{4\upsilon}$ is the factor group for tetragonal BT crystal, the sunk symmetry of the unit cell leads to each of the F_{1u} modes to split into $A_1 + E$, whereas the F_{2u} modes also splits, into $B_1 + E$. The bands at 77, 169, 260, 307, 518, and 717 cm^{-1} are corresponding to E(TO), $\{A_1(TO), E(TO), A_1(LO), E(LO)\}$, $A_1(TO)$, $\{B_1, E(TO + LO)\}$, $\{E(TO), A_1(TO)\}$, and $\{E(LO),$
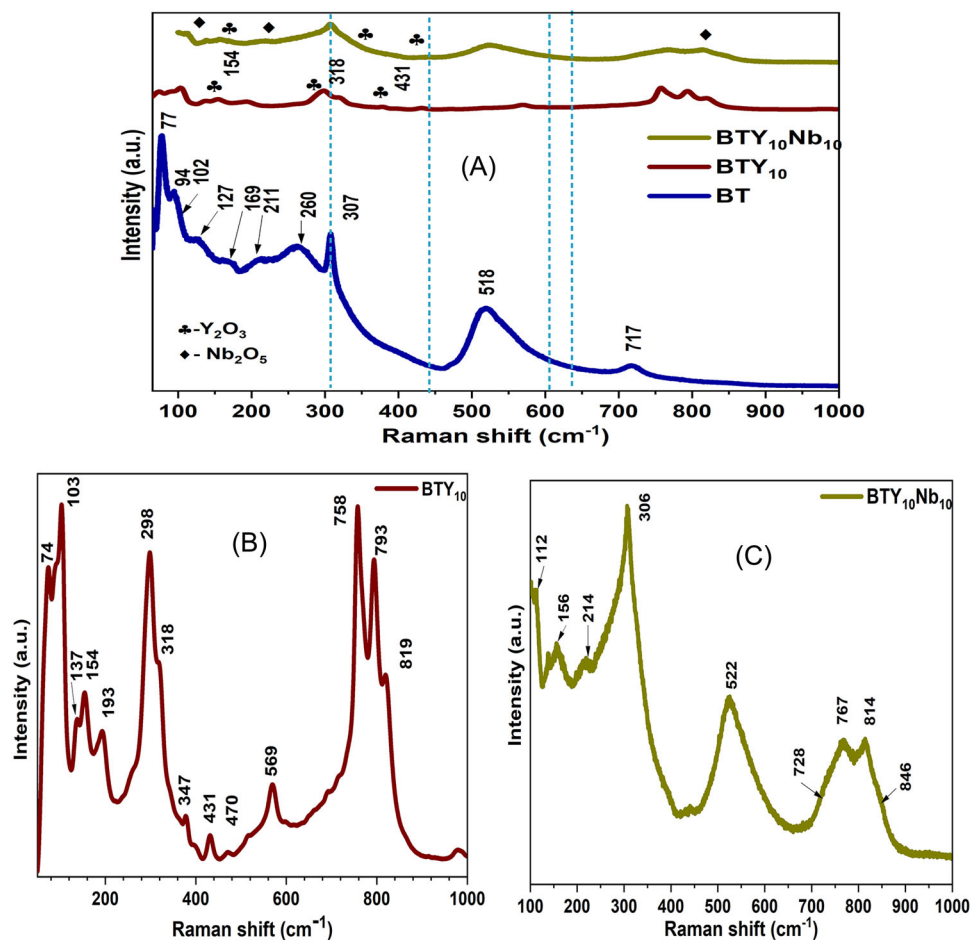
FIGURE 3 Raman spectra of (A) BT, BTY_{10}, and $BTY_{10}Nb_{10}$ ceramics, (B) BTY_{10}, and (C) $BTY_{10}Nb_{10}$

$A_1(LO)$}, respectively, phonon modes were revealed for BT as displayed in Figure 3A. A sharp band of about 307 cm^{-1} was found associated to {B_1, E(TO + LO)} phonon mode of tetragonal BT crystal.[20–23] Most of the BTY_{10} and $BTY_{10}Nb_{10}$ bands were unveiled similar to those detected by BT, despite some band shifts presented in Figure 3B,C.

The band of BT at 307 cm^{-1} showed a slight blue shift of 298 and 306 cm^{-1} for BTY_{10} and $BTY_{10}Nb_{10}$, respectively. The bands 307, 518, and 717 cm^{-1} are found to be broad in these three ferroelectrics. In chemically modified ferroelectrics such as BTY_{10} and $BTY_{10}Nb_{10}$, band splitting is observed in the band of 717 cm^{-1} due to the ionic states Y^{3+}, Nb^{3+}, and Nb^{5+}. When 10 mol% of Y_2O_3 was added to BT, a shift in the lower wavelength region was observed. This may be due to the occupation of Ba^{2+} ionic sites by Y^{3+} sites in the BT crystal lattices. On the other hand, when 10 mol% of Nb_2O_5 was added to BTY_{10}, a band shift from 298 to 306 cm^{-1} is observed toward higher wavelength region, which is due to the presence of Nb. Raman bands of Y_2O_3 were revealed at 154, 318, and 431 cm^{-1} in BTY_{10} powder sample.[24] The bands exposed to 111, 214, and 814 cm^{-1} belong to the Nb_2O_5 dopant of $BTY_{10}Nb_{10}$ ferroelectrics.

3.5 | Morphological studies

3.5.1 | SEM analysis

Typical SEM micrographs of BT, BTY_{10}, $BTNb_{10}$, and $BTY_{10}Nb_{10}$ ceramics were displayed at a resolution scale of 500 nm, as shown in Figure 4. The average grain size of the BT, BTY_{10}, $BTNb_{10}$, and $BTY_{10}Nb_{10}$ samples in one direction were evaluated with the help of histograms as 152.75 nm (Figure 4A), 181 nm (Figure 4B), 148 nm (Figure 4C), and 133.41 nm (Figure 4D), respectively. The average grains of ceramics from SEM images were estimated by using Image-J software is presented in the inset of Figure 4. In $BTY_{10}Nb_{10}$ ferroelectric, it is noticed that the particles were clearly agglomerated with an average grain size of 133.41 nm shown in inset of Figure 4D. These clustering reduce the pores of this ferroelectric sample, then increase the dense microstructure between the particles and improve their ability to store recoverable energy. The average pore area of ferroelectric $BTY_{10}Nb_{10}$ (shown in red) is estimated to be 6.96 nm in the total area of 20.31 nm. Significant homogeneity was also perceived in $BTY_{10}Nb_{10}$
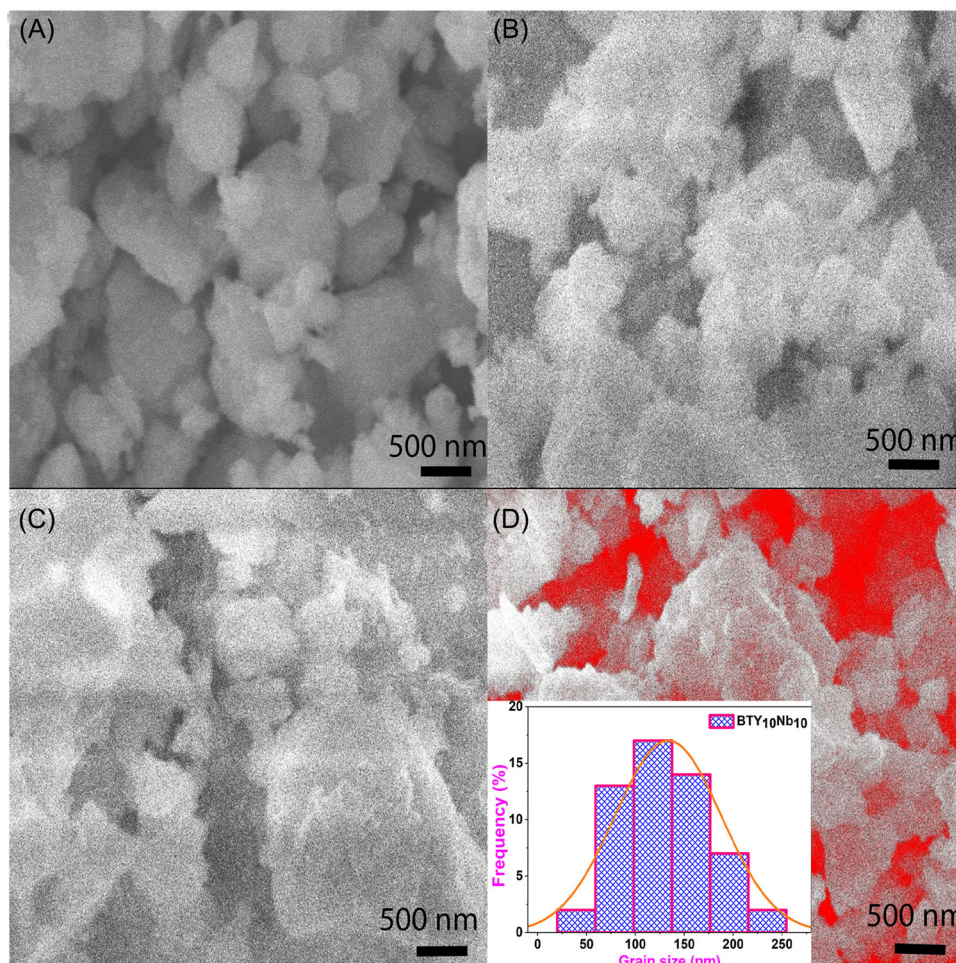
FIGURE 4 Scanning electron microscopy (SEM) images of (A) BT, (B) BTY_{10}, (C) $BTNb_{10}$, and (D) $BTY_{10}Nb_{10}$ with their histograms for particle size

ceramics with few rod--shaped structures compared to BT, BTY_{10}, and $BTNb_{10}$ shown in Figure 4D. Spherical and rod-type surface topology are identified in every sample which is may be due to BT samples.

3.5.2 | TEM analysis

Particle size, size distribution, and morphology of the BTY_2, BTY_{10}, $BTNb_2$, and $BTNb_{10}$ nanopowders from TEM images are presented in Figure 5. At lower concentrations, 2 mol% of Y_2O_3/Nb_2O_5-doped BT (BTY_2 and $BTNb_2$) images revealed highest number of BT nanorods compared to BTY_{10} and $BTNb_{10}$. This is an evidence that the increase in dopant concentration may cause agglomeration of the particles. At higher dopant concentration, compared to $BTNb_{10}$, nanorods are clearly resolved in BTY_{10}. However, BT nanorods were revealed even in the presence of Nb_2O_5 in $BTY_{10}Nb_{10}$ because coexistence of Y_2O_3 concentration helps to reveal few nanorods. Rod-shape morphology in nanosize that are revealed in these samples displayed in

Figure 5A–D. The length of minor axis of the nanorods was estimated on 50 nm scale. The average width of minor axis of the nanorods was around 270 and 100 nm for BTY_{10} and $BTNb_{10}$, respectively. However, these BT nanorods form in small amounts in samples. Additionally, 12 h of grinding and long duration of thermal treatment led to the formation of these nanorods. The presence of nanorods will change the morphology of the $BTY_{10}Nb_{10}$, then increase the surface roughness which may help in enhancing storage capacity of the battery.

3.6 | Dielectric properties

The influence of frequency on dielectric constant, conductivity, and dielectric loss was investigated for the BT, BTY_{10}, and $BTY_{10}Nb_{10}$ samples at room temperature in the frequency range of 0–1 MHz, as shown in Figure 6A–D. Polarization of a dielectric medium is the sum of four types of polarizations such as electronic, ionic, orientation, and space charge polarization, and it is intensely
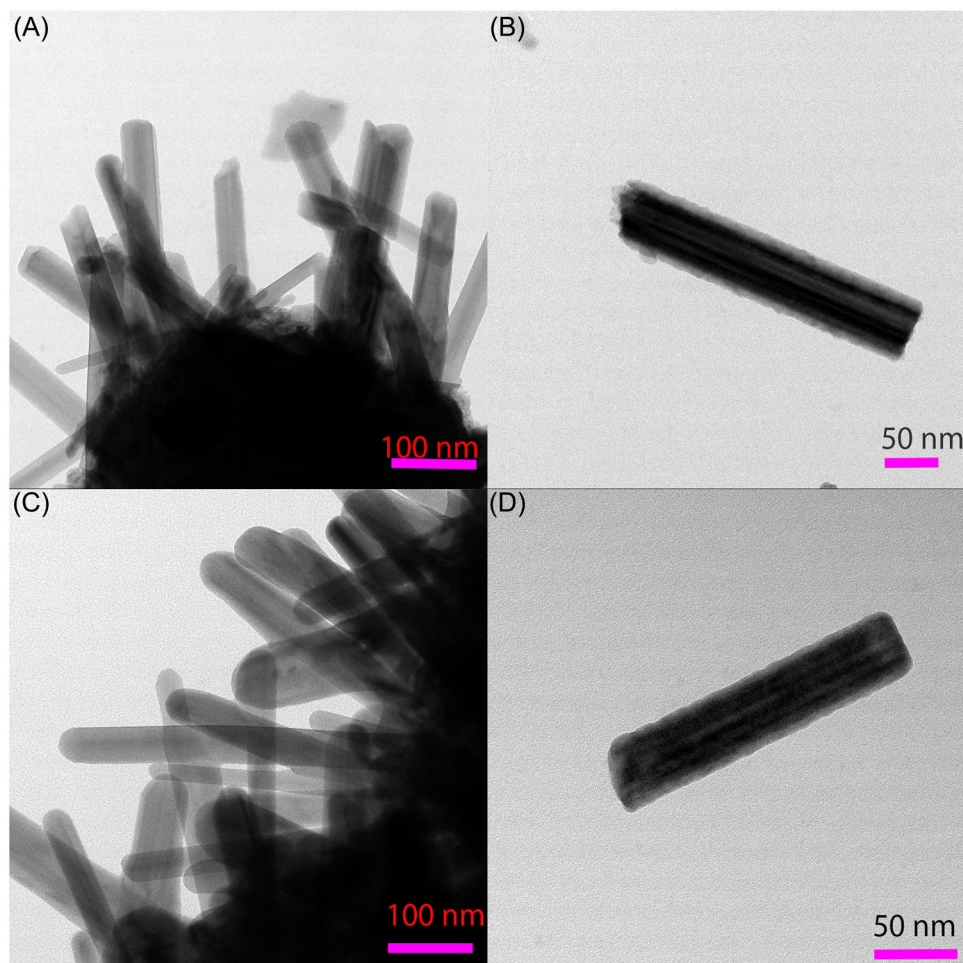
FIGURE 5 Transmission electron microscopy (TEM) images of (A) BTY_2, (B) BTY_{10}, (C) $BTNb_2$, and (D) $BTNb_{10}$

dependent on frequency. At low frequencies, all types of polarization can exist owing to sufficient time to take dipole moment, however, as the frequency is increased various polarizations will filter out. The reason behind this is accredited to the decrease of ε_r with frequency. Below 100 kHz, BT ferroelectric shows a rapid increase in dielectric constant, whereas gradual increase in BTY_{10} and $BTY_{10}Nb_{10}$ due to their chemical modification in the composition that leads to structural modification. The presence of dopant Y^{3+} and Nb^{5+} ions responds slowly at lower frequencies that cause gradual changes in dielectric constant, as shown in Figure 6A, whereas the dielectric constant of BT sample is unaltered at all higher frequencies. However, the charge separation gradually decreases with increasing frequency and then becomes almost constant for all samples at higher frequencies. This is due to the frequency of the electric field applied, which prevents it from dipole moment of the dielectric material. As stated by Arlt et al.'s[25] theory, the grain size (G) of a dielectric material strongly influences its dielectric constant value. As the grain size increases, the width of a ferroelectric

domain (d) increases according to the formula: $G \propto \sqrt{d}$. Furthermore, number of domains with large sized walls would cause the enhancement in dielectric constant.

Figure 6B demonstrates the frequency dependance of electrical conductivity of the BT, BTY_{10}, and $BTY_{10}Nb_{10}$ samples. The conductivity of BT ferroelectric is found to be lower than that of BTY_{10} and $BTY_{10}Nb_{10}$ ferroelectrics. In the case of BTY_{10}, the conductivity increases almost linearly as the frequency increases. On the other hand, for $BTY_{10}Nb_{10}$ ferroelectrics, the conductivity initially increases to 200 kHz and then remains constant at higher frequencies and between the conductivity of BT and BTY_{10}.

Dielectric loss (tan δ) is a dielectric parameter of a dielectric material that quantifies its characteristic dissipation of electromagnetic energy. There is loss of energy as heat originates due to the electrical conduction and orientational polarization of material. Variation in tan δ unveils the same propensity as that of the dielectric constant with frequency. At lower frequencies, tan δ is high in BT and remains low in the BTY_{10} and $BTY_{10}Nb_{10}$
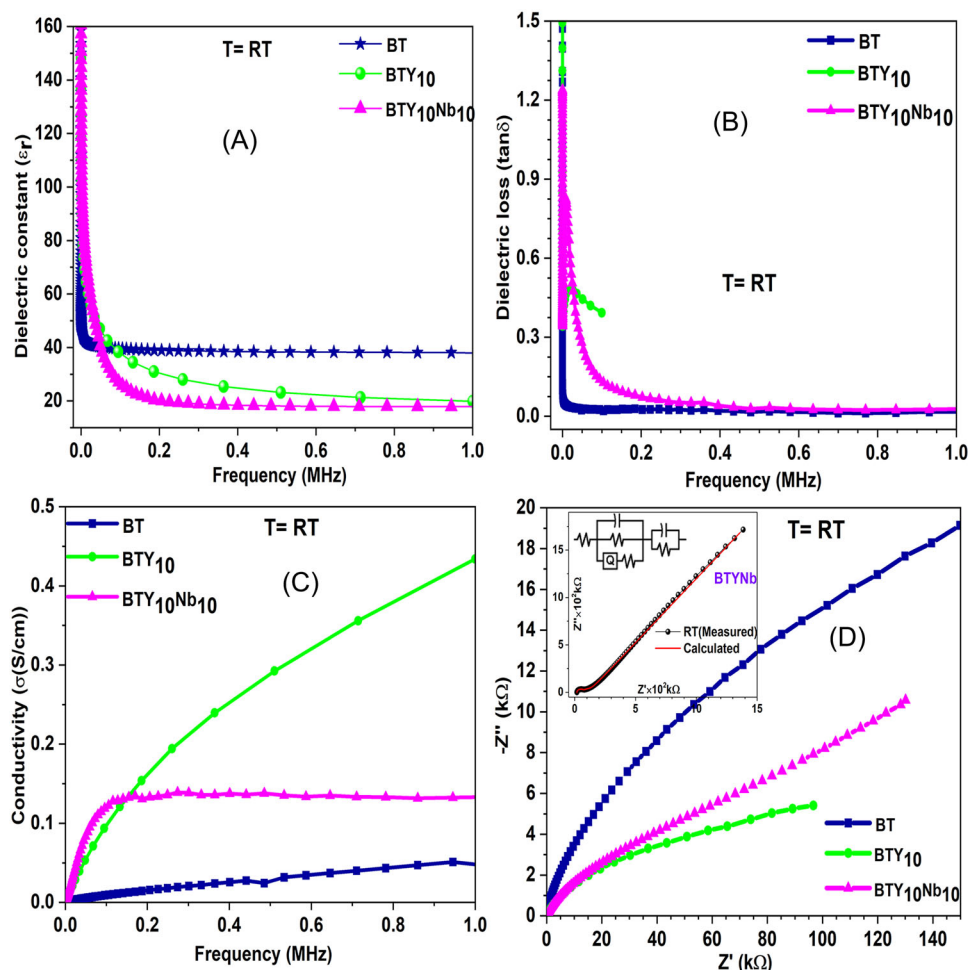
FIGURE 6 Frequency dependence of (A) dielectric constant, (B) dielectric loss, (C) electrical conductivity, and (D) Z' versus Z'' for BT, BTY_{10}, and $BTY_{10}Nb_{10}$ ceramics

samples as displayed in Figure 6C. The motion of electrons cannot be in the direction of applied electric field at higher frequencies, which effects low dielectric loss. BTY_{10} and $BTY_{10}Nb_{10}$ ferroelectrics have shown slight variation at lower frequency compared to BT. At higher frequencies, these samples show similar behavior to that of BT. The observed reduction in dielectric loss of BTY_{10} and $BTY_{10}Nb_{10}$ ceramics is may be due to a reduction in the leakage current through the domain walls, which is in general affected by lattice imperfections like vacancies and dislocations. In contrast, the significant increase in δ or $\tan \delta$ at low frequencies observed for doped BT ferroelectrics is owing to ionic charge imbalance of the materials.[26]

The electrical properties of these samples are usually performed to analyze the impedance of the equivalent circuit and the frequency of the electric field applied. An equivalent circuit of these dielectrics are composed of capacitance (C), inductance (L), resistance (R), and constant phase element (CPE). Some commonly used physical models used to adapt experimental data are

Maxwell–Wagner,[27,28] Hashin–Shtrikman model,[29] effective medium theory,[30] Zuzovsky–Brenner model,[31] Brick Layer model,[32] etc.; the obtained experimental results are described by impedance parameters real (Z') and imaginary (Z'') part. Figure 6D represents the influence of dopant concentration of Y_2O_3 and Nb_2O_5 on BT, as understood from the Nyquist plots of BT, BTY_{10}, and $BTY_{10}Nb_{10}$. In these samples, $BTY_{10}Nb_{10}$ displays an incomplete flattened semicircle at a frequency as low as .1 kHz. The Nyquist plot appears to be composed of two overlapping semicircles as the frequency increased.[33] This separation is resolved more significantly as the frequency increases. In addition, $BTY_{10}Nb_{10}$ exhibited a semicircle at low frequencies, but at high frequencies it showed a slight curvature and then became linear. Conversely, BT and BTY_{10} did not exhibit semicircle behavior at low frequencies, whereas the three samples showed similar behavior at high frequencies. The reason to exhibit semicircle at low frequency of $BTY_{10}Nb_{10}$ is may be because of the addition of Nb_2O_5. The semicircles confirm the existence of non-Debye-type

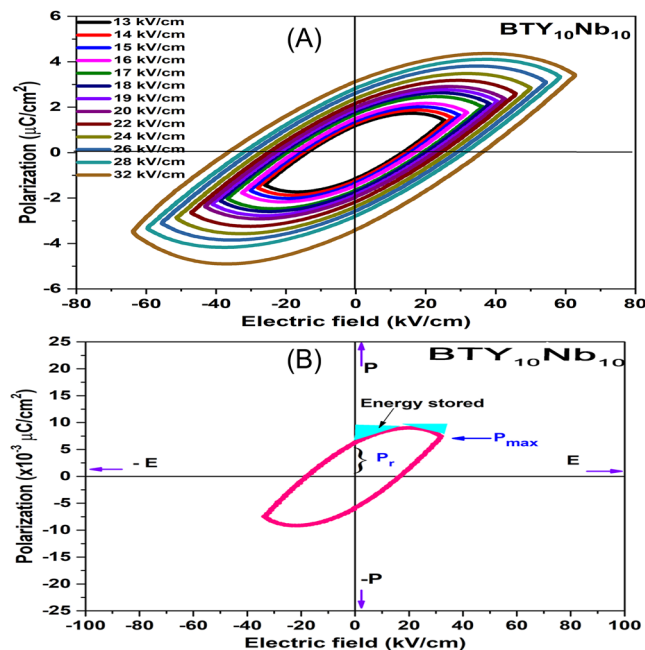**FIGURE 7** $P–E$ curve of the $BTY_{10}Nb_{10}$ sample (A) with different electric fields and (B) with 13 kV/cm at room temperature

relaxation. The expansion of the two semicircles shown in Figure 6D displays grain presence and grain boundary effects. Impedance data simulated using the resistor CPE (R-CPE) equivalent circuit model are shown in the inset of Figure 6D. For non-Debye-type system, CPE is familiarized in the circuit as a substitute of capacitance.

3.7 | Electric hysteresis curve

Polarization versus electric field ($P–E$) curve of the $BTY_{10}Nb_{10}$ sample with different applied electric field and a constant electric field of 13 kV/cm at room temperature indicates the ferroelectric behavior and is presented in Figure 7. From 13 to 32 kV/cm, the $BTY_{10}Nb_{10}$ exhibited ferroelectric behavior with increased hysteresis loss, as shown in Figure 7A. No phase change was observed at various applied electric fields. The electric hysteresis from Figure 7B, P_{max} = .01399 $\mu C/cm^2$, P_r = .0120 $\mu C/cm^2$, $P_{max} - P_r$ = .00197 $\mu C/cm^2$, and E_c = –17.59 kV/cm are evaluated by the instrument. The recoverable energy storage density of $BTY_{10}Nb_{10}$ ferroelectric from the data is W_{rec} = 2.6348 $\mu J/cm^3$ and the energy storage efficiency (η) is 57%. This efficiency is high in $BTY_{10}Nb_{10}$ samples compared to 33.5% for $Ba_{0.997}La_{0.003}TiO_3$,[34] 38.5% for BT,[34] and 53% for (.7-x)$BiFeO_3$-.3$BaTiO_3$-x$Bi(Zn_{2/3}Nb_{1/3})O_3$ + .1wt% Mn_2O (BF–BT–.05BZN)[2]; on the other hand, the efficiency is less as compared to 77% for .5$SrTiO_3$−.5(.95$Bi_{.5}Na_{.5}TiO_3$−.05$BaAl_{.5}Nb_{.5}O_3$) (.5ST−.5(BNT−BAN))[35] and 86.89% for

(1 − x)$BaTiO_3$- x$K_{.73}Bi_{.09}NbO_3$ (.92BT—.08KBN) relaxor ferroelectric ceramics.[5] In general, high W_{rec} is achieved by high P_{max}, low P_r, and large breakdown field using Equation (1). The most promising materials with high energy densities are relaxor–ferroelectric and antiferroelectric materials owing to their high P_{max} and low P_r. The dielectric breakdown strength of the $BTY_{10}Nb_{10}$ sample at room temperature is obtained as .0133.

4 | CONCLUSION

Bare BT and 10 mol% of Y_2O_3-modified BTY_{10} as well as Nb_2O_5 ($BTY_{10}Nb_{10}$) powders were prepared by solid-state reaction method and investigated for structure, morphology, and electrical properties. Glass transition, crystallization temperatures, and weight loss were extracted using TG–DSC analysis. The multi-phases of the compositions with base phase of $BaTiO_3$ were revealed by XRD spectra and depend on the modifier content. FTIR and Raman spectra revealed Ba-, Y-, and Nb-associated vibrational bands and structural phase of the prepared compositions. The porosity (6.96 nm) of $BTY_{10}Nb_{10}$ in relation to battery electrode viability was calculated by Image J software. BT nanorods were confirmed by morphological analysis using TEM that increases surface roughness of the samples. The $BTY_{10}Nb_{10}$ ferroelectric achieved 57% of the recoverable energy storage efficiency for battery applications estimated using ferroelectric hysteresis. These results indicate that structurally and surface topologically modified $BTY_{10}Nb_{10}$ to be a potential ferroelectric material for solid-state energy storage pulsed capacitor applications. Various BT-based nanocomposites are required to develop high dielectric breakdown (more than .0133 of $BTY_{10}Nb_{10}$) to enhance energy storage capacity. Rare earth (Y_2O_3)-based BT shows longer life time of the dielectric capacitor. In addition, further doping of metal oxides such as bismuth oxide, alkali oxides, lanthanum oxide, etc., to this BT-based lead-free composition with slim hysteresis and high energy density would result due to their ferroelectric to relaxor to antiferroelectric phase in making commercially viable capacitors for wide range of energy storage applications.

REFERENCES

1. Brown E, Ma C, Acharya J, Ma B, Wu J, Li J. Controlling dielectric and relaxor-ferroelectric properties for energy storage by tunning $Pb_{0.92}La_{0.08}Zr_{0.52}Ti_{0.48}O_3$ film thickness. ACS Appl Mater Interfaces. 2014;6(24):22417–22.
2. Wang D, Fan Z, Li W, Zhou D, Feteira A, Wang G, et al. High energy storage density and large strain in $Bi(Zn_{2/3}Nb_{1/3})O_3$-doped $BiFeO_3$–$BaTiO_3$ ceramics. ACS Appl Energy Mater. 2018;1(8):4403–12.
3. Liua Z-G, Tang Z-H, Hu S-C, Yao D-J, Sun F, Chen DY, et al. Excellent energy storage density and efficiency in lead-free

Sm-doped $BaTiO_3-Bi(Mg_{0.5}Ti_{0.5})O_3$ ceramics. J Mater Chem C. 2020;8:13405–14.

4. Qi H, Xie A, Tian A, Zuo R. Superior energy-storage capacitors with simultaneously giant energy density and efficiency using nanodomain engineered $BiFeO_3-BaTiO_3-NaNbO_3$ lead-free bulk ferroelectrics. Adv Energy Mater. 2019;10(6):1903338.

5. Lin Y, Li D, Zhang M, Zhan S, Yang Y, Yang H, et al. Excellent energy-storage properties achieved in $BaTiO_3$-based lead-free relaxor ferroelectric ceramics via domain engineering on the nanoscale. ACS Appl Mater Interfaces. 2019;11:36824–30.

6. Huang W, Chen Y, Li X, Wang G, Liu N, Li S, et al. Ultra-high recoverable energy storage density and efficiency in barium strontium titanate-based lead-free relaxor ferroelectric ceramics. Appl Phys Lett. 2018;113:203902.

7. Wang G, Li J, Zhang X, Fan Z, Yang F, Feteira A, et al. Ultra-high energy storage density lead-free multilayers by controlled electrical homogeneity. Energy Environ Sci. 2019;12:582–8.

8. Patel S, Chauhan A, Vaish R. Improved electrical energy storage density in vanadium-doped $BaTiO_3$ bulk ceramics by addition of $3BaO-3TiO_2-B_2O_3$ glass. Energy Technol. 2015;3(1):70–6.

9. Zhi J, Chen A, Zhi Y, Vilarinho PM, Baptista JL. Incorporation of yttrium in barium titanate ceramics. J Am Ceram Soc. 1999;82(5):1345–8.

10. Prakash Jwalaa J, Subohib O, Malik MM. Influence of B-site modification by hetrovalent (Nb^{5+}) and isovalent (Zr^{4+}) dopants in $BaTiO_3$ on its dielectric and electrical properties synthesized by novel sol gel route. Mater Res Express. 2019;6(9): 096308.

11. Appiah M, Hao H, Liu Z, Jiang X, Emmanuel M, Abdullah J, et al. A unique mechanism for dielectric-temperature stability of $BaTiO_3$-based ceramics using $Ba(OH)_2/TiO_2$ suspension. J Phys Chem C. 2020;124(26):14089–98.

12. Louaer A, Chaguetmi S, Taibi A, Layachi A, Satha H. Crystallization kinetics and growth mechanism of 0.5 $(Ba_{0.85} Ca_{0.15})TiO_3-0.5$ Ba $(Zr_{0.1} Ti_{0.9})$ O_3 powders prepared via solid-state reaction. Phase Transit. 2019;93(1):116–33.

13. Ansaree MJ, Upadhyay S. Thermal analysis of formation of nano-crystalline $BaTiO_3$ using $Ba(NO_3)_2$ and TiO_2. Process Appl Ceram. 2015;9(4):181–5.

14. Hao S, Fu D, Li J, Wang W, Shen B. Preparation and Characterization of Ag-Doped BaTiO3 Conductive Powders. Int J of Inorg Chem. 2011;2011:1–4.

15. Akbas HZ, Aydin Z, Karahan IH, Dilsizoglu T, Turgut S. Process control using FT-IR analysis of $BaTiO_3$ from ultrasonically activated $BaCO_3$ and TiO_2. In: Proceedings of 17th Research World International Conference (IMSEC 2016), Riyadh, Saudi Arabia. 2016. ISBN: 978-93-86083-37-1.

16. Ashiri R. Detailed FT-IR spectroscopy characterization and thermal analysis of synthesis of barium titanate nanoscale particles through a newly developed process. Vib Spectrosc. 2013;66:24–9.

17. He K, Chen N, Wang C, Wei L, Chen J. Method for determining crystal grain size by X-ray diffraction. Cryst Res Technol. 2018;53(2):1700157.

18. Weidenthaler C. Pitfalls in the characterization of nanoporous and nanosized materials. Nanoscale 2011;3:792.

19. Khan M, Mishra A, Shukla J, Sharma P. X-ray analysis of $BaTiO_3$ ceramics by Williamson–Hall and size strain plot methods. AIP Conf Proc. 2019;2100:020138.

20. Lazarevi Z, Rom·cevi N, Vijatovi M, Paunovi N, Rom·cevi M, Stojanovi B, et al. Characterization of barium titanate ceramic powders by Raman spectroscopy. Acta Phys Pol A. 2009;115(9):808–10.

21. Busca G, Buscaglia V, Leoni M, Nanni P. Solid-state and surface spectroscopic characterization of $BaTiO_3$ fine powders. Chem Mater. 1994;6:955–61.

22. Shiratori Y, Pithan C, Dornseiffer J, Waser R. Raman scattering studies on nanocrystalline $BaTiO_3$ Part II – consolidated polycrystalline ceramics. J Raman Spectrosc. 2007;38:1300–6.

23. García-Hernández M, Chadeyron G, Boyer D, García-Murillo A, Carrillo-Romo F, Mahiou R. Hydrothermal synthesis and characterization of europium-doped barium titanate nanocrystallites. Nano-Micro Lett. 2013;5(1):57–65.

24. Yuan G, Li M, Yu M, Tian C, Wang G, Fu H. In situ synthesis, enhanced luminescence and application in dye sensitized solar cells of $Y_2O_3/Y_2O_2S:Eu^{3+}$ nanocomposites by reduction of $Y_2O_3:Eu^{3+}$. Sci Rep. 2016;6:37133.

25. Arlt G, Hennings D, de With G. Dielectric properties of fine grained barium titanate ceramics. J Appl Phys. 1985;58:1619.

26. Jain A, Panwar AK. Synergetic effect of rare-earths doping on the microstructural and electrical properties of Sr and Ca Co-doped $BaTiO_3$ nanoparticles. Ceram Int. 2020;46(8):10270–8.

27. Maxwell JC. A treatise on electricity and magnetism. Oxford: Clarendon Press; 1881.

28. Wagner KW. The after effect in dielectrics. Arch Electrotech Berlin. 1914;2:378.

29. Hashin Z, Shtrikman S. A variational approach to the theory of the effective magnetic permeability of multiphase materials. J Appl Phys. 1962;33:3125–31.

30. Bruggeman DAG. Berechnung verschiedener physikalischer konstanten von heterogenen substanzen. Ann Phys (Leipzig). 1935;24:636–79.

31. Zuzovsky M, Brenner H. Effective conductivities of composite materials composed of cubic arrangements of spherical particles embedded in an isotropic matrix. J Appl Math Phys. 1977;28: 979–92.

32. van Dijk T, Burgraaf AJ. Grain boundary effects on ionic conductivity in ceramic $Gd_x,Zr_{l-x},O_{2-(x/2)}$, solid solutions. Phys Stat Sol (a). 1981;63:229.

33. Starczewska A, Toro B, Szperlich P, Nowak M. Electrical property analysis of textured ferroelectric polycrystalline antimony sulfoiodide using complex impedance spectroscopy. Materials 2021;14:2579.

34. Puli VS, Li P, Adireddy S, Chrisey DB. Crystal structure, dielectric, ferroelectric and energy storage properties of La-doped $BaTiO_3$ semiconducting ceramics. J Adv Dielectr. 2015;5(3):1550027.

35. Yan F, Yang H, Lin Y, Wang T. Dielectric and ferroelectric properties of $SrTiO_3-Bi_{0.5}Na_{0.5}TiO_3-BaAl_{0.5}Nb_{0.5}O_3$ lead-free ceramics for high-energy-storage applications. Inorg Chem. 2017;56:13510–6.